Lawrence Berkeley National Laboratory
LBL Publications

Title

XtalCAMP: A comprehensive program for the analysis and visualization of scanning Laue X-ray micro-/nanodiffraction data

Permalink

https://escholarship.org/uc/item/63v0q5rp

Journal

Journal of Applied Crystallography, 53(5)

ISSN

0021-8898

Authors

Li, Y
Chen, K
Dang, X
et al.

Publication Date

2020-10-01

DOI

10.1107/S1600576720010882

Peer reviewed

eScholarship.org Powered by the California Digital Library
University of California

electronic reprint

JOURNAL OF APPLIED CRYSTALLOGRAPHY

ISSN: 1600-5767
journals.iucr.org/j

XtalCAMP: a comprehensive program for the analysis and visualization of scanning Laue X-ray micro-/nanodiffraction data

Yao Li, Kai Chen, Xiaofeng Dang, Fengying Zhang, Nobumichi Tamura, Ching-Shun Ku, Huijun Kang and Hans-Rudolf Wenk

J. Appl. Cryst. (2020). **53**, 1392–1403

IUCr Journals
CRYSTALLOGRAPHY JOURNALS ONLINE

Copyright © International Union of Crystallography

Author(s) of this article may load this reprint on their own web site or institutional repository provided that this cover page is retained. Republication of this article or its storage in electronic databases other than as specified above is not permitted without prior permission in writing from the IUCr.

For further information see https://journals.iucr.org/services/authorrights.html

JOURNAL OF APPLIED CRYSTALLOGRAPHY
ISSN 1600-5767

XtalCAMP: a comprehensive program for the analysis and visualization of scanning Laue X-ray micro-/nanodiffraction data

Yao Li,[a,b] Kai Chen,[b]* Xiaofeng Dang,[b] Fengying Zhang,[a] Nobumichi Tamura,[c] Ching-Shun Ku,[d] Huijun Kang[e] and Hans-Rudolf Wenk[f]

[a]School of Materials Science and Engineering, Chang'an University, Xi'an, Shaanxi 710064, People's Republic of China, [b]Center for Advancing Materials Performance from the Nanoscale (CAMP-Nano), State Key Laboratory for Mechanical Behavior of Materials, Xi'an Jiaotong University, Xi'an, Shaanxi 710049, People's Republic of China, [c]Advanced Light Source, Lawrence Berkeley National Laboratory, Berkeley, CA 94720, USA, [d]National Synchrotron Radiation Research Center, Hsinchu, Taiwan 30076, People's Republic of China, [e]Key Laboratory of Solidification Control and Digital Preparation Technology (Liaoning Province), School of Materials Science and Engineering, Dalian University of Technology, Dalian 116024, People's Republic of China, and [f]Department of Earth and Planetary Science, University of California, Berkeley, CA 94720, USA. *Correspondence e-mail: kchenlbl@gmail.com

Received 10 April 2020
Accepted 7 August 2020

Edited by A. Borbély, Ecole National Supérieure des Mines, Saint-Etienne, France

Keywords: scanning Laue X-ray micro-/nanodiffraction; computer programs; crystal orientation maps; strain/stress analysis; texture analysis.

XtalCAMP is a software package based on the MATLAB platform, which is suitable for, but not limited to, the analysis and visualization of scanning Laue X-ray micro-/nanodiffraction data. The main objective of the software is to provide complementary functionalities to the Laue indexing software packages used at several synchrotron beamlines. The graphical user interfaces allow the easy analysis of characteristic microstructure features, including real-time intensity mapping for a quick examination of phase, grain and defect distribution, 2D color-coded mapping of microstructural properties from the output of other Laue indexing software, crystal orientation visualization, grain boundary characterization based on orientation/misorientation calculation, principal strain/stress analysis, and strain ellipsoid representation, as well as a series of additional toolkits. As an example, *XtalCAMP* is applied to the microstructural investigation of a solution-heat-treated Ni-based superalloy manufactured using a laser 3D-printing technique, and a deformed natural quartzite from Val Bregaglia in the Central Alps.

1. Introduction

Taking advantage of brilliant synchrotron sources, the scanning Laue X-ray micro-/nanodiffraction (μXRD) technique has become an indispensable high-throughput approach for linking multiscale microstructures to physical properties in statistically large areas of samples with excellent spatial (as good as tens of nanometres) (Lee *et al.*, 2020) and angular resolution (∼0.001°) (Chen, Dejoie *et al.*, 2016; Zhou *et al.*, 2018). With the μXRD technique, the sample is raster scanned under a focused polychromatic X-ray beam and the diffraction pattern (*i.e.* Laue pattern, LP) at each scan spot is recorded using a 2D detector with a short exposure time (0.1–1 s) depending on the intensity of the synchrotron X-ray beam. The spatial distributions of phases, crystal orientation, elastic strains/stresses and microstructural defects can then be extracted after analyzing the LPs. Efficient data analysis software, capable of indexing thousands of diffraction patterns automatically, has thus been a necessity for the popularization of the μXRD technique.

Previous computer programs, such as *LAUEGEN* (Campbell, 1995), *LaueX* (Soyer, 1996) and *OrientExpress* (Laugier & Filhol, 1993), have been designed for Laue

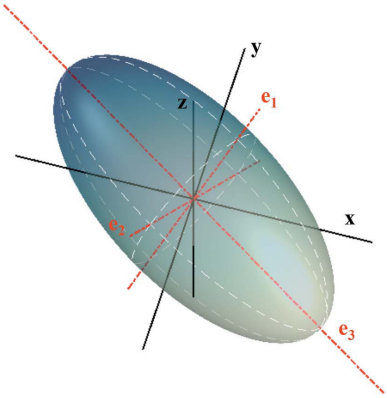

© 2020 International Union of Crystallography

electronic reprint

diffraction data analysis but aimed at isolated LP indexing and crystal orientation determination. This initiated the development of in-house software at synchrotron beamlines to analyze thousands of LPs sequentially, such as the *X-ray Microdiffraction Analysis Software* (*XMAS*) (Tamura, 2014) on beamline 12.3.2 of the Advanced Light Source (ALS) and beamline 21A of the Taiwan Photon Source, *LaueGo* (Liu *et al.*, 2004) on beamline 34-ID-E of the Advanced Photon Source (APS), and *LaueTools* (Robach *et al.*, 2014) on beamline CEA-CNRS BM32 of the European Synchrotron Research Facility. Although structured into different computer formats, the core outputs of these software packages are similar, comprising a matrix of the same dimension and size as the performed scan. Each element of the matrix contains the crystallographic and microstructural information obtained from analysis of the corresponding LP, including the local crystal orientation, strain/stress tensor, LP background intensity, and diffraction peak number and shape. The crystal orientation is usually expressed in one or several of the following ways: orientation matrix, Euler angles, Rodrigues' rotation axis/angle pair and quaternions. The background intensity is an average value of all pixels on the 2D LP. The average FWHM of all indexed Laue peaks in angular space is taken to describe the diffraction peak shape. With these powerful software packages, μXRD has been applied to the investigation of phase identification and structural evolution of micro-/nanocrystals (Guo *et al.*, 2011; Strelcov *et al.*, 2012; Dejoie *et al.*, 2014), orientation mapping of single- or polycrystalline materials (Chen *et al.*, 2010; Ma *et al.*, 2015), transient and residual strain/stress measurement in engineering and natural materials (Chen *et al.*, 2009, 2015, 2020; Li, Xie *et al.*, 2018), and evaluation of dislocation type, arrangement and density by analyzing the Laue peak shape (Lupinacci *et al.*, 2015; Li, Chen & Tamura, 2018). In these typical applications of the μXRD technique, it is found that the functionalities, such as 2D map plotting, misorientation computing, grain boundary characterization and strain/stress distribution visualization, need to be further enhanced for general users.

Therefore, we introduce here a comprehensive custom-developed program, *Crystal Calculating, Analyzing and Mapping Program* (*XtalCAMP*), for in-depth analysis of the output of μXRD data indexing. It incorporates a variety of easy-to-use features, including tools for diffraction intensity study, basic 2D map plotting, crystal orientation and misorientation analysis, grain boundary characterization, strain/stress distribution visualization, and other tasks. As mentioned above, the core information generated from indexing software packages such as *XMAS*, *LaueGo* and *LaueTools* is essentially the same. Here we take the *XMAS* `*.seq` file and *LaueGo* `*.xml` file as examples, but *XtalCAMP* can be applied to the output of other software after the necessary changes in format.

2. Technical description, availability and requirements

XtalCAMP is coded through the MATLAB graphical user interface (GUI) module and can be executed on MATLAB R2014b and higher versions installed on Windows 7 and 10 operating systems (32 bit or 64 bit). It has been registered at the Copyright Protection Centre of China (Registration No. 2016SR060878). The software is available online at http://nano.xjtu.edu.cn/info/1171/2793.htm.

3. Program functionality and features

The general architecture and principal functions of *XtalCAMP* are shown in Fig. 1. The diffraction intensity can be extracted and mapped with *XtalCAMP* for qualitative microstructure imaging, independent of *XMAS* or any other LP indexing/analysis software. The output of LP indexing software packages [either in ASCII (`*.txt`) or specific binary `*.seq` formats generated by *XMAS*] can be directly imported into *XtalCAMP*, and 2D maps can then be plotted for microstructure imaging using various colorbars and user-defined threshold filters. Finally, further data processing can be performed, including the plotting of pole figures, inverse pole figures, ordinary grain boundaries, twin boundaries and misorientation distributions. In addition, *XtalCAMP* provides some other useful toolkits for data analysis, as summarized in Fig. 1.

To demonstrate the basic data processing functions of *XtalCAMP*, a μXRD study of a heat-treated DZ125L Ni-based superalloy manufactured by laser 3D printing is adopted as an example. A precipitation-hardened superalloy fabricated by directional solidification was selected as the substrate. Three kinds of phases exist in this alloy: the γ-austenite matrix, $L1_2$-ordered γ'-$Ni_3(Al, Ti, Ta)$ precipitates and *M*C-type carbides. Powders of the same compositions as the substrate were laser clad on the (001) plane of the substrate. With the aid of a high thermal gradient applied antiparallel to the building direction, columnar grains with a width of ~500 μm grew in epitaxy with the bottom substrate, extending to multiple cladding layers. Due to high dislocation densities and residual strain/stress, complete recrystallization occurred in the heat-affected zone (HAZ) after post-manufacturing solution heat treatment at 1513 K for 2 h. The μXRD experiment was carried out at the ALS on beamline 12.3.2 (Kunz *et al.*, 2009). A area of 570 × 300 μm on the longitudinal section of the heat-treated sample was raster scanned using the microfocused X-ray beam with a 3 μm step

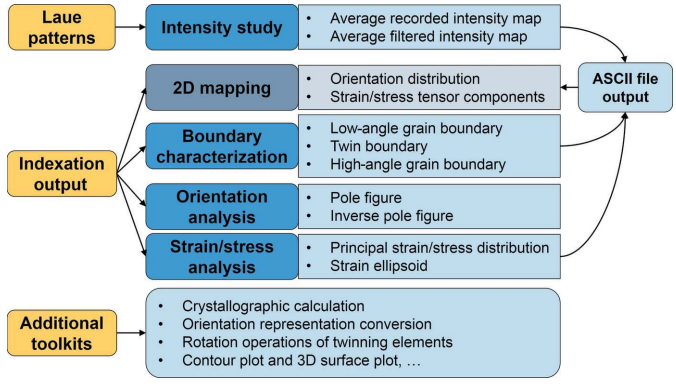

Figure 1
The architecture of *XtalCAMP*.

electronic reprint

size, covering the substrate and the cladding layers. Finally, a total of 19 000 LPs were automatically indexed with *XMAS*, taking advantage of the newly developed peak position comparison (PPC) indexing algorithm (Kou *et al.*, 2018), and the indexing outputs (`*.seq` format) were imported into *XtalCAMP* for further analysis. All LPs were indexed using the crystal structure of nickel, due to the small misfit and cube-on-cube orientation relationship between the γ and γ' phases (Li, Chen & Tamura, 2018).

In addition, a tectonically deformed natural quartzite sample was studied using the μXRD technique and then the residual strain distribution was visualized with *XtalCAMP*. The sample was collected from Val Bregaglia in the Central Alps, sliced into petrographic thin sections with a thickness of ∼30 μm and mounted on a glass slide. An area of 501 × 501 μm with a 3 μm step size was scanned using the micro-focused polychromatic X-ray beam in the same reflection geometry as used for the laser 3D-printed Ni alloy on beamline 12.3.2 at the ALS (Wenk *et al.*, 2020) with 27 889 LPs.

Details of the sample preparation and μXRD experiments are described in Appendix *A*.

3.1. Diffraction intensity analysis and mapping

As indexing thousands of LPs in a scan is time consuming, we developed a novel approach to collect the intensity of each LP without indexing, facilitating a quick overview of characteristic microstructural features, including cracks, voids, dendrite structures, precipitates and grain boundaries, in a real-time manner. The following lists the main steps of this approach, which can be automatically accomplished with the 'Read Average Intensity' interface under the 'Tools' menu in the main interface of *XtalCAMP*, as shown in Fig. 2(*a*):

(i) For a μXRD scan, an LP is recorded at each position using a 2D detector. The dimensions of the detector, XDim (n) and YDim (m), need to be input into the software [red circles in Fig. 2(*a*)]. The average recorded intensity I_R for an individual LP is defined by averaging the gray values of all pixels in this pattern, that is

$$I_R = \frac{\sum_{k=1}^{nm} I_r^k}{nm}, \tag{1}$$

where I_r^k is the gray value of the kth pixel.

(ii) To enhance the microstructural contrast, treatment is required to distinguish LPs with different peak shapes. The approach adopted here is to set a threshold intensity (I_t) for each LP, which is defined as $I_t = C_f I_R$. C_f is a defined filter factor, which is constant for all the LPs taken in the whole scanned area, and by default C_f is equal to 4. The reason why this method works has been explained in our previous publication (Zhou *et al.*, 2016).

(iii) The filtered intensity I_f^k of the kth pixel is defined as

$$I_f^k = \begin{cases} 0 & \text{when } I_r^k \le I_t, \\ I_r^k - I_t & \text{when } I_r^k > I_t. \end{cases} \tag{2}$$

Then, the averaged filtered intensity I_F of an individual LP is obtained by averaging the filtered intensity of all the pixels in the LP:

$$I_F = \frac{\sum_{k=1}^{nm} I_f^k}{nm}, \tag{3}$$

(iv) Finally, by setting the path where the LPs are stored and pressing 'Run', the average recorded intensity I_R and averaged filtered intensity I_F of all the LPs are saved as a `*.txt` file in a user-defined directory, which can be imported into *XtalCAMP* and visualized as a 2D map plot. Details of the import and plot operations are introduced in Sections 3.2 and 3.3, respectively. Here an example is given to demonstrate how the microstructure features are studied from the maps of the average recorded and filtered intensities.

The average recorded intensity map in Fig. 2(*b*) displays the morphology of the sample surface, while the averaged filtered

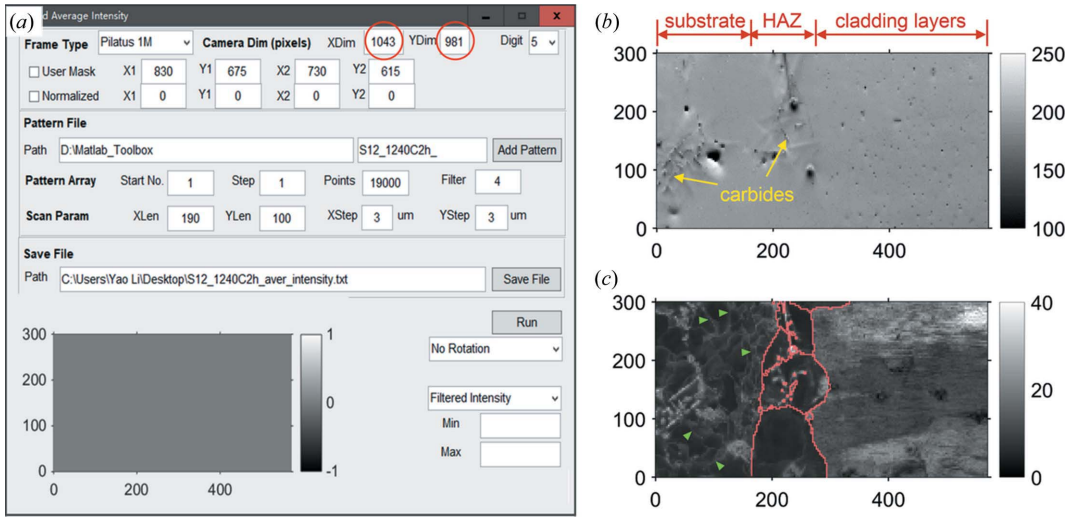

Figure 2
Diffraction intensity analysis and mapping before LP indexing. (*a*) Snapshot of the diffraction intensity study interface. (*b*) Average recorded intensity map. (*c*) The average filtered intensity map is obtained by a default filter factor of 4, where the HAGBs are outlined in red and the LAGBs are denoted by green triangles. The coordinate units are micrometres.

electronic reprint

intensity map in Fig. 2(*c*) shows the more detailed microstructure features of the Ni-based superalloy sample. Due to the enrichment of heavy elements and sharp diffraction peaks, *M*C-type carbides (*M* = W, Ta, Ti) in the substrate and the HAZ give stronger intensity signals. In addition, some boundary features, which are identified as low-angle grain boundaries (LAGBs) in Section 3.5, are observed in the substrate as darker contrast, because of the peak splitting of the LPs collected in these regions. As for the completely recrystallized area in the HAZ, the crystal orientation (and thus Laue peak indices and intensity) becomes significantly different from the substrate and the cladding layers, resulting, through contrast, in the clear visualization of high-angle grain boundaries (HAGBs). The non-uniform contrast in the cladding layers is attributed to the local orientation gradient and microstructural defects. The contrast of both images can be adjusted by setting the range (minimum and maximum) of the grayscale values.

3.2. Data input

The file input function is achieved in the main window of *XtalCAMP*, as displayed in Fig. 3. The input data can be the µXRD results, diffraction intensity analysis output or other ASCII files such as fluorescence data which are occasionally collected when µXRD experiments are performed. The µXRD results are the most frequently used in *XtalCAMP* so we will take them as an example. They can be provided either in text format of the output matrix from the LP indexing software packages or via the binary `*.seq` file generated specifically by *XMAS* after automatically processing thousands of LPs collected in raster scan mode. To read a *LaueGo* `*.xml` file, a toolkit named 'Read APS LaueGo XML File' (as shown in Fig. 4) has been developed and is accessible under the 'Tools' menu to convert a `*.xml` file to a plain text file. In this window, *x* and *y* coordinates need to be assigned from the columns Xsample, Ysample or Depth. Users can also define

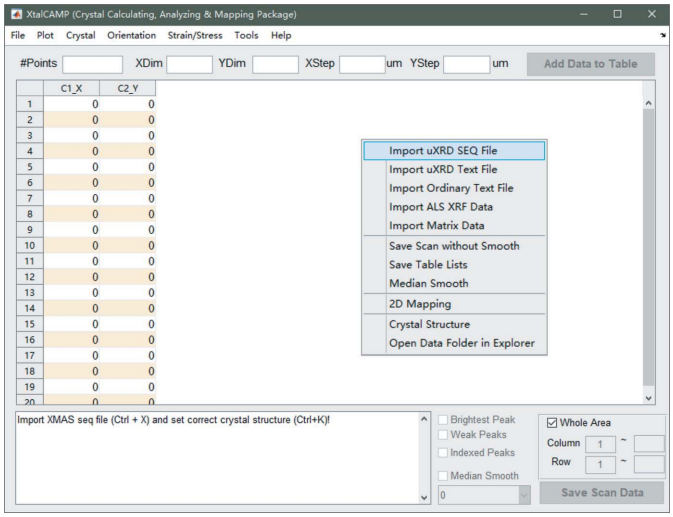

Figure 3
The main window of *XtalCAMP*, showing the right-click options.

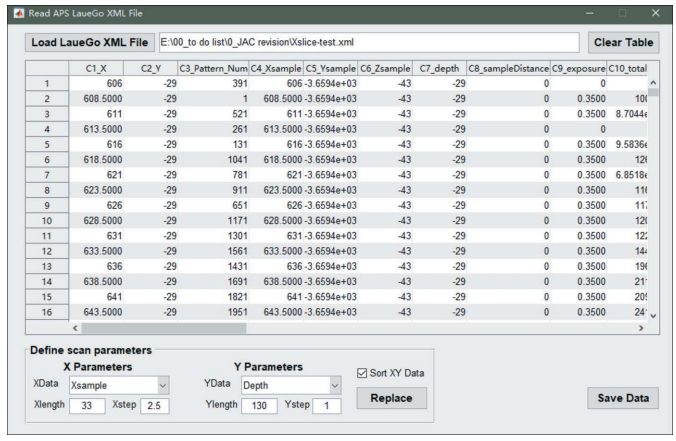

Figure 4
The 'Read APS LaueGo XML File' window designed for converting a `*.xml` file to a plain text file.

the *x* and *y* coordinates by the total scan spot numbers (Xlength and Ylength) and step sizes (Xstep and Ystep) along the *x* and *y* directions. Afterwards, a table can be saved as a text file and re-loaded into *XtalCAMP* through the main interface (Fig. 3) for further analysis.

After loading, either through the 'File' menu or the right-click context menu, a table appears on the screen with the same number of rows as LPs (Fig. 3). Each row is composed of grain information derived from the indexing results of an LP, including scan spot coordinates, pattern number, diffraction geometry parameters, orientation matrix values, strain/stress tensor components, average peak width *etc.*, which then allows the construction of 2D maps of the distribution of a certain microstructural feature.

3.3. 2D color-coded mapping

The *x* and *y* coordinates of each scanning position are automatically calculated according to the scanning stage positions in the `*.seq` file and are by default displayed in the first two columns when the data are loaded into *XtalCAMP*, and then a certain aspect of the microstructure characteristics at the location of the grid sites specified by the *x* and *y* coordinates can be visualized by plotting the 2D color-coded (including grayscale) map using the corresponding column entry. Although this is a built-in functionality of LP indexing programs such as *XMAS*, *LaueGo* or *LaueTools*, users have limited permissions to change the display style of the map. In the 2D color-coded mapping interface of *XtalCAMP* (Fig. 5), various options are available for users to self-define the map appearance, such as color styles, color ranges, visualization of not-indexed pixels in different colors from the colorbar, filter selections for data colored in the map, axis label settings and gray shade for skipped data (in 'Missdata Color'). The data cursor is designed to read the pixel value from the map.

In Fig. 5, the average peak width, which is the averaged FWHM of all Laue peaks indexed in a single LP, is taken as an example. As the peak width reflects the local dislocation concentration, the heterogeneous distribution indicates a

electronic reprint

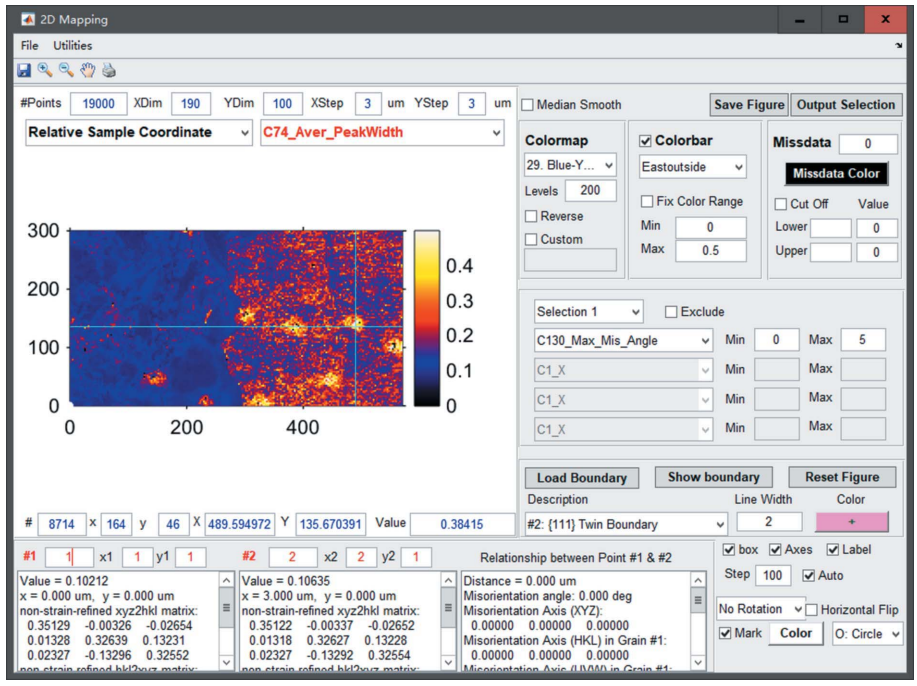

Figure 5
A snapshot of the 2D color-coded mapping interface.

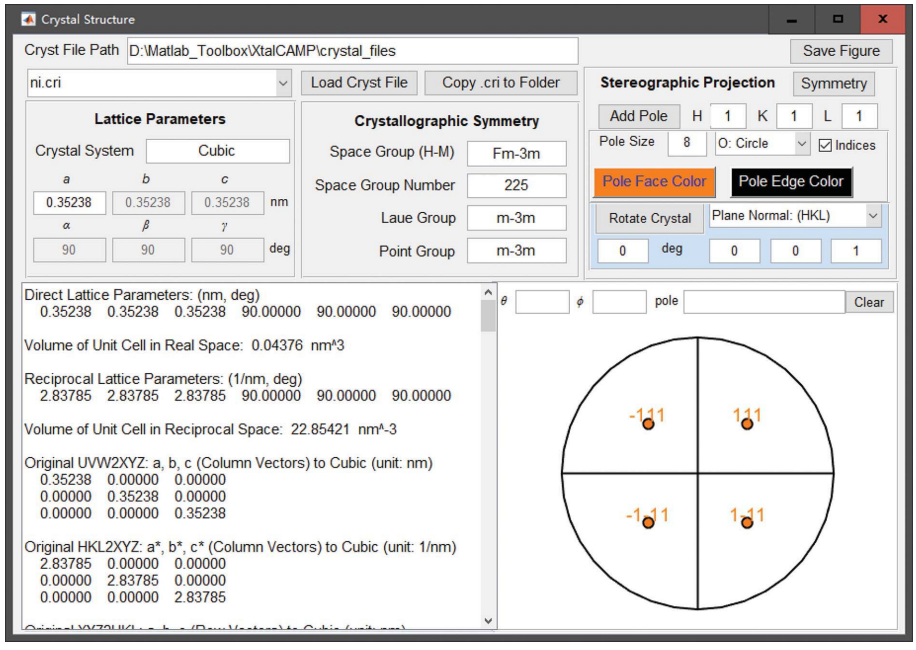

Figure 6
The crystal structure selection interface of *XtalCAMP*.

relatively larger population of dislocations stored in the cladding layers, in spite of the disappearance of dendrite structure after solution heat treatment.

3.4. Crystal selection

As no crystal structure information is contained in the `*.seq` file or other `*.txt` files, one needs to pre-set the crystal structure for the crystal orientation/misorientation analysis. In this case, one can access the 'Crystal' menu in the main window (Fig. 3) and select the correct crystal file via the window shown in Fig. 6. *XtalCAMP* supports both the standard crystallographic information file (`*.cif`) and the crystal file (`*.cri`) defined by *XMAS*, from which the unit cell and basic information about the crystal structure can be obtained. The two formats can be converted to each other using *XtalCAMP*. Once a certain crystal structure is selected, the space-

electronic reprint

group and point-group annotations are displayed and the crystal symmetry is represented by the stereographic projection of the (001) pole center in the lower-right corner of the window. The atomic coordinates, relevant to the diffraction intensity, are listed in the text box in the lower-left corner of the window.

For crystallographic calculations (*e.g.* the angle between two crystal vectors) in a certain (cubic or non-cubic) crystal structure, it is convenient to define a Cartesian coordinate system $\mathbf{a}^{o}\mathbf{b}^{o}\mathbf{c}^{o}$, in which $\mathbf{a}^{o}$, $\mathbf{b}^{o}$ and $\mathbf{c}^{o}$ are unit vectors perpendicular to each other and adherent to the generally non-Cartesian crystal lattice coordinate system **abc**. On the basis of the common definition, the relationship between the two coordinates follows (Matthies *et al.*, 1988)

$$\mathbf{c}^{o} \parallel \mathbf{c}, \quad \mathbf{b}^{o} \parallel \mathbf{c} \times \mathbf{a}, \quad \mathbf{a}^{o} \parallel \mathbf{b}^{o} \times \mathbf{c}^{o}, \tag{4}$$

where the $\times$ denotes the cross product of two vectors. Therefore, there exists a coordinate transformation matrix **L** (Liu & Liu, 2012)

$$\mathbf{L} = \begin{bmatrix} a\sin\beta & b(\cos\gamma - \cos\alpha\cos\beta)/\sin\beta & 0 \\ 0 & b(1-\cos^2\alpha-\cos^2\beta-\cos^2\gamma \\ & \quad +2\cos\alpha\cos\beta\cos\gamma)^{1/2}/\sin\beta & 0 \\ a\cos\beta & b\cos\alpha & c \end{bmatrix}, \tag{5}$$

where a, b, c, α, β and γ are the unit-cell parameters. It is apparent that the coordinates of the lattice vectors **a**, **b** and **c** correspond to the columns of **L**. Similarly, the rows of $\mathbf{L}^{-1}$ (the inverse matrix of **L**) are the coordinates of the lattice vectors **a***, **b*** and **c*** in reciprocal space. Therefore, the arbitrary indices of a crystal direction or plane in the coordinate system **abc** can be readily converted into the coordinate system $\mathbf{a}^{o}\mathbf{b}^{o}\mathbf{c}^{o}$ using the **L** matrix and vice versa, where the conversion equations are given by He & Jonas (2007). As shown in Fig. 6, matrices **L** and $\mathbf{L}^{-1}$ and other crystal information are displayed in the text box in the lower-left corner.

3.5. Orientation and misorientation analysis

In the *XMAS* `*.seq` file, the crystal orientation is represented by the **xyz2hkl** matrix, and its transpose matrix is denoted by **G**, which describes the rigid rotation from the Cartesian coordinate system $\mathbf{a}^{o}\mathbf{b}^{o}\mathbf{c}^{o}$ to the sample coordinate system **xyz** by a rotational operation **R**:

$$\mathbf{G} = \mathbf{xyz2hkl}^{\mathrm{T}} = \mathbf{RL} = \begin{pmatrix} a_x & b_x & c_x \\ a_y & b_y & c_y \\ a_z & b_z & c_z \end{pmatrix}, \tag{6}$$

where the elements of matrix **G** represent the projections of the lattice vectors **a**, **b**, **c** on the x, y and z axes in the sample coordinate system. The **R** matrix is a pure rotation matrix, which is equivalent to a set of three Euler angles in the Bunge setting widely adopted in texture analysis (Bunge, 1969; Kocks *et al.*, 1998; Engler & Randle, 2009) and in electron backscatter diffraction (EBSD) software. Similarly to the transformation matrix **L**, the vectors and Miller indices in the coordinate system **abc** can be converted into the coordinate system **xyz** using the **G** matrix and vice versa.

The misorientation matrix **M** between two crystal orientations $\mathbf{G}_1$ and $\mathbf{G}_2$ is derived as

$$\mathbf{M} = \mathbf{G}_1\mathbf{G}_2^{-1} = \mathbf{R}_1\mathbf{L}\mathbf{L}^{-1}\mathbf{R}_2^{-1} = \mathbf{R}_1\mathbf{R}_2^{-1}, \tag{7}$$

where $\mathbf{R}_i$ is the corresponding rotation matrix of $\mathbf{G}_i$ ($i = 1$ or 2). The misorientation matrix **M** is also a rotation matrix, which can be represented as a misorientation angle–axis pair. By checking the misorientation between adjacent scan spots, the boundary configurations, such as LAGBs, twin boundaries (TBs) and HAGBs, in the scan area can be identified.

In *XtalCAMP*, the misorientation angle–axis pair $\{\theta_r, \mathbf{v}_r\}$ between the current spot P and its right neighbor P_r and $\{\theta_u, \mathbf{v}_u\}$ between P and its upper neighbor P_u are calculated (Fig. 7).

Then the boundary configurations are identified following the procedure below:

(i) An LAGB is formed if the misorientation angle θ_r is smaller than a threshold angle ω_g (user-defined but commonly set as 15°), while the lower bound of θ_r lacks rigorous definition and is usually dependent on the angular resolution. For μXRD technique, the lower bound of θ_r can be set as 0.1°, which is 100 times larger than the angular resolution.

(ii) If the misorientation angle θ_r is larger than ω_g, the boundary is characterized as an HAGB, but in many cases it is of interest whether it is a special boundary, such as a TB, or an ordinary HAGB. We have reported a look-up-table-based approach to achieve this function (Li, Wan & Chen, 2015). Firstly, a look-up table which lists all the misorientation angle–axis pairs $\{\theta_t, \mathbf{v}_t\}$ is established considering the given twin law (either mirror plane or twin axis/angle) and the rotational symmetry operations associated with the selected crystal structure. Then the boundary is identified as a TB if the measured misorientation meets the following two conditions simultaneously:

$$|\theta_r - \theta_t| < \omega_{t1} \quad \text{and} \quad \theta_v < \omega_{t2}, \tag{8}$$

where ω_{t1} and ω_{t2} are user-defined threshold angles taking into account the inherent uncertainties in orientation measurement and the plastic deformation effect, and θ_v is the angle between $\mathbf{v}_r$ and $\mathbf{v}_t$. Otherwise, if θ_r is larger than ω_g and the conditions in equation (8) are not satisfied, the boundary is identified as an HAGB.

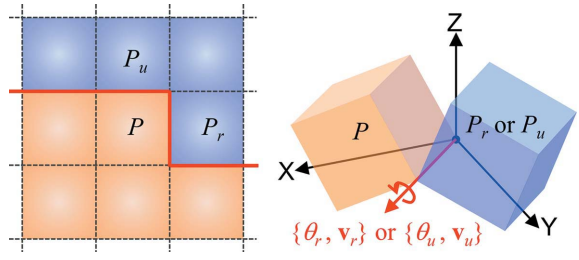

Figure 7
Schematic illustration of the grain boundary characterization algorithm.

electronic reprint

(iii) The same analysis procedure is repeated to check the boundary between P and P_u.

By extending the process to the entire scan, the measured misorientation angle–axis pairs and boundary information are output as two `*.txt` files. There is also an option to output a `*.cpt` file with Bunge Euler angles as used in the *BEARTEX* software (Wenk *et al.*, 1998) which can be used for texture analysis.

We again use the 3D-printed Ni-based superalloy data as an example. After re-loading the two `*.txt` files generated from the misorientation angle–axis pair calculation and grain boundary configuration identification into *XtalCAMP*, an RGB inverse pole figure map (without showing the program interface) and misorientation map are plotted (Fig. 8) with TBs and HAGBs superimposed in different colors. As shown in Fig. 8(*a*), HAZ grains are visualized in different colors from the substrate and cladding layers, demonstrating the occurrence of recrystallization in the HAZ after solution heat treatment due to the large amount of stored energy from the high density of dislocations (Chen *et al.*, 2020). It is observed in Fig. 8(*b*) that the dislocation density becomes low and a {111} twin forms on recrystallization. In addition, the LAGBs in the substrate (denoted by green triangles) are consistent with the contrast found in the average filtered intensity map in Fig. 2(*c*), while more LAGBs with higher misorientation angles are detected in the cladding layers, consistent with previous studies (Xue *et al.*, 2015; Li *et al.*, 2020).

It is convenient to read the orientation matrix using the data cursor in the 2D color-coded map. As seen in Fig. 8, on clicking the two grains next to the TB (marked by a blue circle and triangle in the figure), their orientation information is listed in the bottom text boxes, and the misorientation between them is automatically calculated and shown in the third text box. The misorientation is close to $\{60^\circ, [\bar{1}11]\}$, validating our TB identification algorithm. The {111} twin relationship can be further confirmed from the {111} pole figure, which is implemented in the interface shown in Fig. 9. The 111 poles of these two orientations are displayed in different colors. The overlapped $\bar{1}11$ poles of the two grains show that they share the same $(\bar{1}11)$ plane, which serves as the mirror plane between the twin and parent domains.

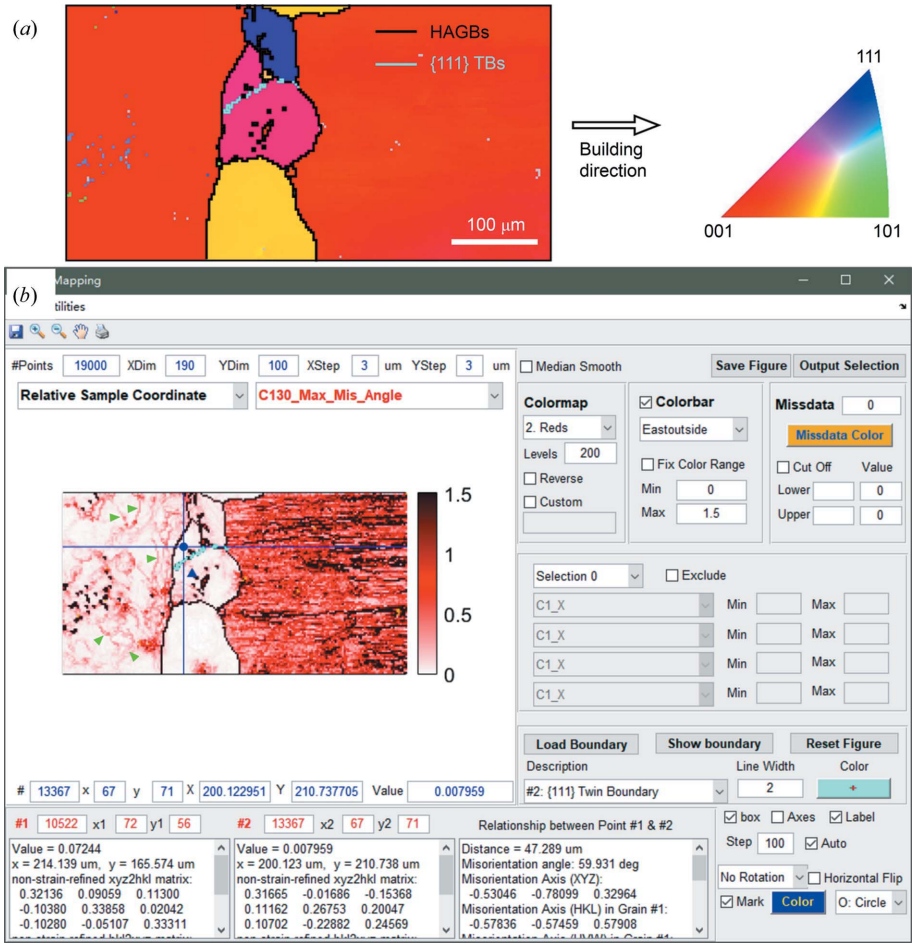

Figure 8
Orientation and misorientation maps obtained by *XtalCAMP*. (*a*) RGB inverse pole figure map along the building direction, which is rotated by 90° counter-clockwise. (*b*) The 2D color-coded mapping interface, showing HAGBs (dark lines) and {111} TBs (cyan lines) superimposed on the misorientation angle map. The color scale and the color of the grain/twin boundaries can be selected from the panels to the right of the map.

3.6. Strain/stress analysis

For polychromatic X-ray Laue diffraction, the wavelength of each peak is unknown and the volumetric change of the unit cell is thus indeterminable. However, the lattice distortion can be detected based on the hypothesis of constant volume of the unit cell. Therefore, the dilatational strain tensor $\boldsymbol{\delta}$ is undetectable, while the deviatoric strain tensor $\boldsymbol{\varepsilon}'$ (3×3 matrix, $\boldsymbol{\varepsilon}' = \boldsymbol{\varepsilon} - \boldsymbol{\delta}$, where $\boldsymbol{\varepsilon}$ is the full strain tensor) can be determined from the slight shift in Laue peak positions relative to the unstrained crystal. It is common practice to compute the deviatoric stress tensor $\boldsymbol{\sigma}'$ by applying Hooke's law: $\boldsymbol{\sigma}' = \boldsymbol{C}\boldsymbol{\varepsilon}'$, where $\boldsymbol{C}$ is the fourth-rank stiffness tensor. Note that this calculated $\boldsymbol{\sigma}'$ is the deviatoric stress tensor only when the studied crystal is cubic. For non-cubic crystals, the calculated $\boldsymbol{\sigma}'$ is slightly different from the true deviatoric stress tensor, although in most cases it is a good approximation. Details can be found in Appendix *B*. The deviatoric strain/stress tensor components are contained in the output from the μXRD data processing software file (*e.g.* `*.seq`) and can be visualized by the 2D color-coded

electronic reprint

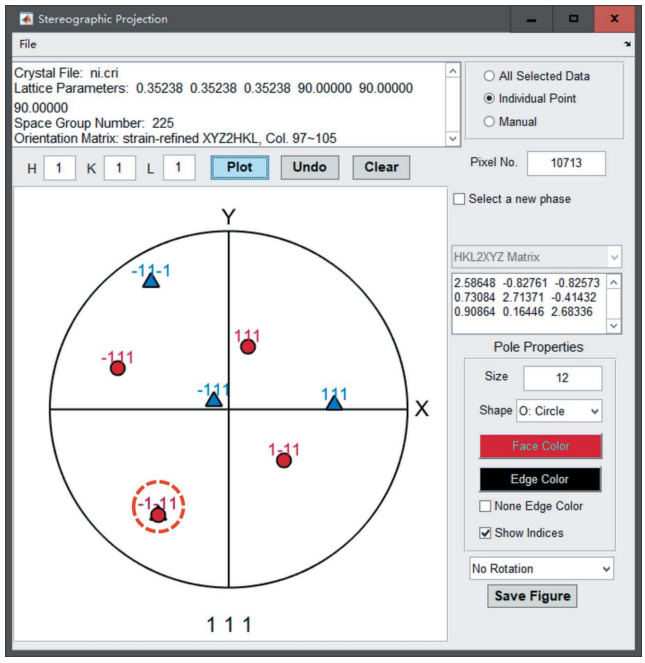

Figure 9
A {111} stereographic projection of the two scan spots marked in Fig. 8(*b*). The overlapped poles are marked by the red dashed circle.

mapping interface (Fig. 5). Frequently, it is necessary to express the strain or stress tensor in different coordinate systems. For example, a strain tensor $\boldsymbol{\varepsilon}_{x'y'z'}$ in O–$x'y'z'$ coordinates can be obtained by rotating a tensor $\boldsymbol{\varepsilon}_{xyz}$ in O–xyz coordinates:

$$\boldsymbol{\varepsilon}'_{x'y'z'} = \mathbf{R}\boldsymbol{\varepsilon}'_{xyz}\mathbf{R}^{\mathrm{T}}, \tag{9}$$

where $\mathbf{R}$ is a rotation matrix denoting the rotation from O–xyz to O–$x'y'z'$ coordinates. For this purpose, *XtalCAMP* provides a convenient toolkit for the user to calculate the strain/stress tensor after rotation.

With respect to a strained/stressed crystal, there are three mutually perpendicular planes where the shear strain/stress components are 0 but only normal strain/stress components exist. The three normal strains/stresses are called principal strains/stresses, and the corresponding strain/stress directions are normal to these three principal planes. Under the 'Strain/Stress' menu in the main window of *XtalCAMP* (Fig. 3), the functionality to calculate the principal strains/stresses and their directions are stored as a `*.txt` file, which can be re-loaded into *XtalCAMP*. The magnitudes and directions of principal strains of the second-rank deviatoric strain tensor $\boldsymbol{\varepsilon}'$ can be obtained by calculating the eigenvalues and eigenvectors (Noyan & Cohen, 2013):

$$\boldsymbol{\varepsilon}'_{\mathrm{p}} = \begin{pmatrix} \varepsilon'_{\mathrm{p1}} & 0 & 0 \\ 0 & \varepsilon'_{\mathrm{p2}} & 0 \\ 0 & 0 & \varepsilon'_{\mathrm{p3}} \end{pmatrix} = \mathbf{T}^{\mathrm{T}}\boldsymbol{\varepsilon}'\mathbf{T}, \tag{10}$$

where $\boldsymbol{\varepsilon}'_{\mathrm{p}}$ represents the principal strain tensor, $\varepsilon'_{\mathrm{p1}}$, $\varepsilon'_{\mathrm{p2}}$ and $\varepsilon'_{\mathrm{p3}}$ the three principal strains in ascending order, and $\mathbf{T}$ the rotation matrix composed of three column eigenvectors. In the case of the deviatoric strain tensor, the summation of $\varepsilon'_{\mathrm{p1}}$, $\varepsilon'_{\mathrm{p2}}$ and $\varepsilon'_{\mathrm{p3}}$ (the trace of $\boldsymbol{\varepsilon}'_{\mathrm{p}}$) is 0, which means $\varepsilon'_{\mathrm{p1}}$ is always compressive while $\varepsilon'_{\mathrm{p3}}$ is always tensile (except when all components are 0). This is also valid for deviatoric stresses.

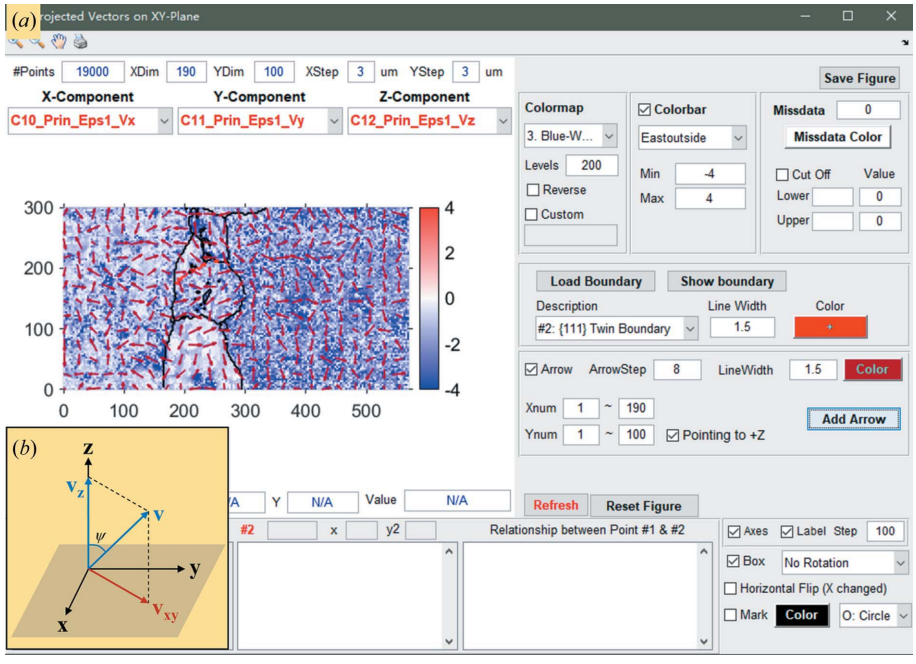

Figure 10
The principal strain visualization interface. (*a*) Arrows denoting the compression strain axis direction superimposed on the magnitude distribution map of principal compression strain in the laser 3D-printed Ni-based superalloy. (*b*) A schematic diagram showing an arbitrary vector projected on the *xy* plane.

In order to show the magnitude and direction of the principal strain simultaneously, superimposition of the strain direction projection on the 2D color-coded principal strain map is adopted, as seen in Fig. 10(*a*). As schematically displayed in Fig. 10(*b*), for the projection vector $\mathbf{v}_{xy}$ of an arbitrary strain direction $\mathbf{v}$, the length of $\mathbf{v}_{xy}$ can reflect the magnitude of the z component of $\mathbf{v}$. For an overview of the strain direction distribution, the $\mathbf{v}_{xy}$ of every nth (n is a user-defined variable which is 8 in this example) scan spot is denoted by an arrow in Fig. 10(*a*). This approach has been successfully applied to explain the residual strain distribution in alloys and minerals (Li, Qian *et al.*, 2015; Chen, Kunz *et al.*, 2016).

Additionally, the strain ellipsoid is used to demonstrate the magnitude and orientation of the strain field. As seen in Fig. 11, $\mathbf{e}_1$, $\mathbf{e}_2$ and $\mathbf{e}_3$ denote the principal strain directions and the dashed ellipses delineate the corresponding principal planes. It is clear that the rotation matrix $\mathbf{T}$ in equation (10) represents the

electronic reprint

Table 1
Additional tools in *XtalCAMP*.

Application	Crystallographic study	Orientation/misorientation calculation	Data visualization
Tools	1. Equivalent directions and Miller indices	1. Conversion of different orientation representations	1. Contour plot
	2. Conversion of three-digit indices to four-digit indices for hexagonal and trigonal symmetry	2. Misorientation between two **xyz2hkl** matrices by considering the rotational symmetry	2. 3D surface plot
	3. Angle between two vectors	3. Construction of look-up table for twin identification	3. Inverse pole figure
	4. Conversion between plane indices and the plane normal direction		4. Misorientation profile along a line
			5. Frequency statistics of microstructural properties

rotational operation between $e_1e_2e_3$ coordinates and the sample coordinates xyz. As a result, the strain ellipsoid can be treated as an 'orthorhombic crystal' with three main axes, the minor axis e_1 corresponding to compression, the major axis e_3 corresponding to tension and the intermediate axis e_2. In this way, the compressive and tensile strain axis distribution can be visualized by ⟨100⟩ and ⟨001⟩ pole figures of such an 'orthorhombic crystal', respectively, either from the orientation matrix as in *XtalCAMP* or by converting the orientation matrix into Euler angles for use in other software such as *BEARTEX*. In *XtalCAMP*, the calculated principal strain magnitude and strain axes and the Euler angles defining the orientation of the strain ellipsoid can be stored as an individual `*.txt` file.

To validate the wider applicability of this approach, naturally deformed quartzite samples with trigonal crystal symmetry were studied by μXRD with a potential use as a paleo-piezometer (Chen, Kunz *et al.*, 2016; Wenk *et al.*, 2020). The residual strain distribution of a quartzite sample is shown in Fig. 12 (for more details see Appendix *A*2). There is a relatively uniform magnitude of residual strain in the scanned area [Figs. 12(*a*) and 12 (*b*)], and the compressive strain vectors are mainly aligned along the *y* axis while the majority of tensile strain vectors are parallel to the *x* axis. The 3D orientation of strain vectors is further expressed by the strain pole figures shown in Figs. 12(*c*) and 12(*d*). Clearly, the compressive strain is aligned nearly parallel to the *y* axis, while the tensile strain is close to the *x* axis, consistent with the projection vector distributions in Figs. 12(*a*) and 12(*b*).

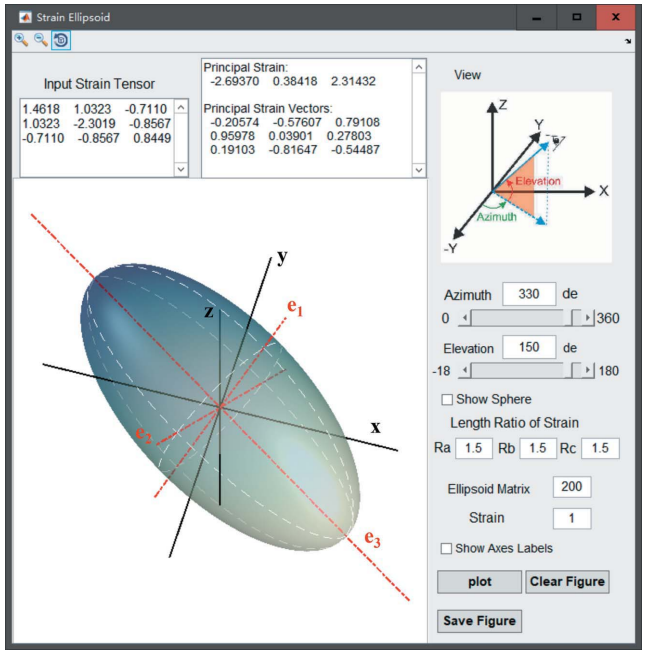

Figure 11
Strain Ellipsoid interface. The principal strain axes are denoted e_1, e_2 and e_3 in red and the sample coordinates are denoted x, y, z in black.

3.7. Additional tools

In addition to the functionalities introduced above, *XtalCAMP* provides many other useful tools, which are straightforward to use. These are listed in Table 1.

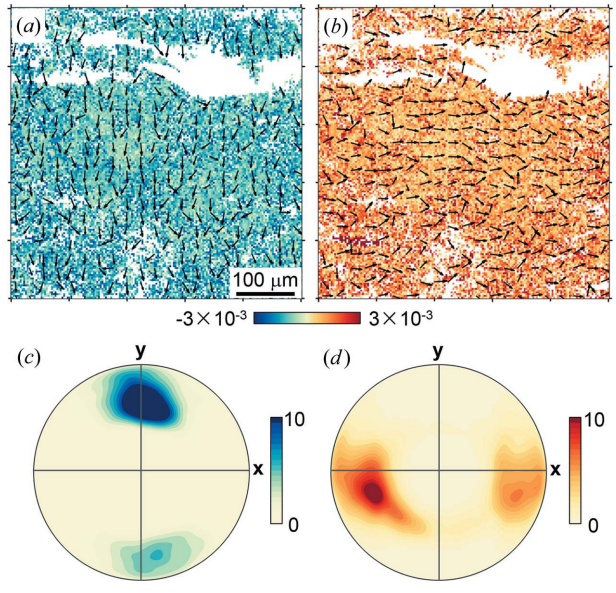

Figure 12
The residual strain distributions in the quartzite sample. The magnitude of the principal (*a*) compressive strain and (*b*) tensile strain and the corresponding strain axis directions are denoted by arrows in every eighth pixel. (*c*) ⟨100⟩ and (*d*) ⟨001⟩ strain pole figures in equal area projection. The arrows indicate the +**z** direction of the vector. The white regions in (*a*) and (*b*) represent the LPs which could not be indexed as quartz (such as a large muscovite mica crystal on top) or were excluded due to severe plastic deformation. Strain units are microstrains and pole figure densities are in multiples of a random distribution.

electronic reprint

4. Conclusions and future outlook

In this article, we have described the implementation of *XtalCAMP*, a comprehensive and versatile program dedicated to post-processing of LP indexing software output.

XtalCAMP provides a variety of tools for the visualization and analysis of scanning μXRD data, including intensity-based microstructure characterization, microstructural property mapping, basic crystallographic calculations, grain orientation visualization, boundary characteristic determination, deviatoric strain/stress analysis and principal strain axis representation, as well as some additional toolkits. With the built-in data conversion tools, μXRD orientation measurements can be transformed into a data format compatible with EBSD data analysis software such as the *MTEX* toolbox (Bachmann *et al.*, 2010) and other programs for quantitative texture analysis such as *BEARTEX*. This will help extend the μXRD technique to more users and adapt the trend that μXRD has been merging with other advanced crystal/materials characterization techniques such as EBSD and high-resolution powder diffraction.

APPENDIX *A*
Sample preparation and μXRD experiment

A1. Laser 3D-printed Ni-based superalloy sample

The thin-wall Ni-based superalloy sample was 3D-printed using an in-house-developed co-axial laser cladding apparatus equipped with a 1 kW Nd:YAG laser source (Do *et al.*, 2013). The substrate was cut from a directionally solidified Ni-based superalloy DZ125L ingot. The DZ125L powders, with particle diameters ranging from 40 to 120 μm, were used as the feedstock and deposited on the (001) plane of the substrate with a fixed laser power of 180 W and a scan rate of 10 mm s^{-1} protected with an Ar atmosphere. The Ar gas-carried powders were injected into the melt pool at a feeding rate of ∼9 mm^3 s^{-1} and the layer thickness was controlled to about 100 μm. After post-processing solution heat treatment at 1513 K for 2 h, a slice with a thickness of ∼1.5 mm was cut longitudinally and investigated by scanning electron microscopy (SEM) in backscattered electron (BSE) mode (Fig. 13) after mechanical grinding and electropolishing.

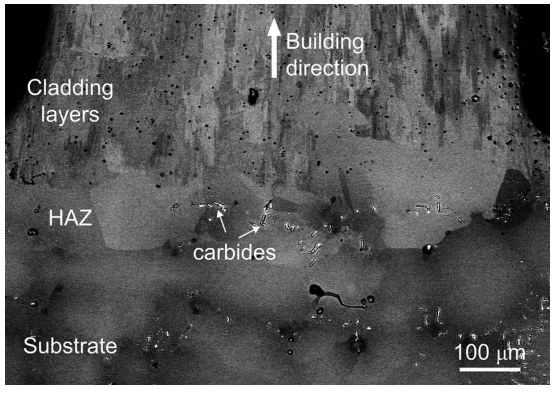

Figure 13
BSE SEM investigation of the laser 3D-printed Ni-based superalloy DZ125L after solution heat treatment.

The heat-treated sample was then examined in a synchrotron Laue μXRD experiment on beamline 12.3.2 at the ALS. The sample was mounted 90° rotated around the surface normal with respect to the SEM image on a high-precision *XY* stage (so that the building direction points towards the right), with a 45° inclination angle between the sample surface normal and the incident X-ray beam. Using a focused polychromatic X-ray beam with a size of ∼1 μm and an energy bandpass between 5 and 24 keV, a total of 19 000 LPs were collected via a 2D detector (Pilatus 1M, 1043 × 981 pixels) from an area of 570 × 300 μm, which covered the substrate, HAZ and cladding layers, with a 3 μm step size on the sample surface. Subsequently, all the LPs were sequentially indexed by the *XMAS* software, taking advantage of the newly developed peak position comparison indexing algorithm.

A2. Deformed quartzite sample

The quartzite sample, collected from Val Bregaglia in the Central Alps, was deformed under greenschist facies metamorphic conditions during the Alpine orogeny 20–60 M years ago (Wenk *et al.*, 2020). From the sample, a thin section with a thickness of ∼30 μm was prepared and mounted on a glass slide. A synchrotron Laue μXRD experiment was performed on beamline 12.3.2 at the ALS and the diffraction patterns were recorded from an area of 501 × 501 μm with a 3 μm step size in a reflection geometry that was the same as that used for the Ni-based superalloy study described above. The experimental geometry parameters, including the detector distance, orientation and incident X-ray beam position, were calibrated using a defect-free synthetic quartz single crystal. For an LP of a trigonal crystal with a hexagonal lattice, the diffraction intensities are taken into account for unambiguous indexing (Chen *et al.*, 2012). The microstructure of the quartzite sample is shown in Fig. 14.

APPENDIX *B*
The calculation of deviatoric stress

The full strain tensor $\boldsymbol{\varepsilon}$ is the sum of the deviatoric strain tensor $\boldsymbol{\varepsilon}'$ and the dilatational strain tensor $\boldsymbol{\delta}$, which can be written out in matrix notation as

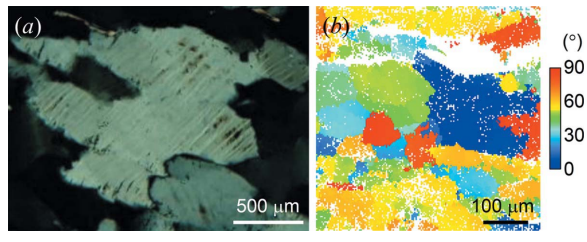

Figure 14
Microstructures of the quartzite sample. (*a*) Microstructure observed with optical microscopy and crossed polarized light. (*b*) The Bunge Euler angle (Φ) distribution of μXRD measurements showing the grain structure.

electronic reprint

$$\begin{pmatrix} \varepsilon_{11} & \varepsilon_{12} & \varepsilon_{13} \\ \varepsilon_{12} & \varepsilon_{22} & \varepsilon_{23} \\ \varepsilon_{13} & \varepsilon_{23} & \varepsilon_{33} \end{pmatrix} = \begin{pmatrix} \varepsilon_{11}-\delta & \varepsilon_{12} & \varepsilon_{13} \\ \varepsilon_{12} & \varepsilon_{22}-\delta & \varepsilon_{23} \\ \varepsilon_{13} & \varepsilon_{23} & \varepsilon_{33}-\delta \end{pmatrix} + \begin{pmatrix} \delta & 0 & 0 \\ 0 & \delta & 0 \\ 0 & 0 & \delta \end{pmatrix}. \quad (11)$$

According to Hooke's law, the full stress tensor $\boldsymbol{\sigma}$ is derived by multiplying the stiffness tensor $\boldsymbol{C}$ and the full strain tensor $\boldsymbol{\varepsilon}$,

$$\boldsymbol{\sigma} = \boldsymbol{C\varepsilon} = \boldsymbol{C}(\boldsymbol{\varepsilon}' + \boldsymbol{\delta}) = \boldsymbol{C\varepsilon}' + \boldsymbol{C\delta}. \quad (12)$$

Similarly to the full strain tensor, the full stress tensor $\boldsymbol{\sigma}$ can also be divided into a deviatoric stress tensor $\boldsymbol{\sigma}'$ and a hydrostatic stress tensor $\boldsymbol{\sigma}_{\rm H}$:

$$\boldsymbol{\sigma} = \boldsymbol{\sigma}' + \boldsymbol{\sigma}_{\rm H}. \quad (13)$$

Comparing equations (12) and (13), it is concluded that the deviatoric stress tensor $\boldsymbol{\sigma}'$ equals $\boldsymbol{C\varepsilon}'$ only when $\boldsymbol{C\delta}$ is a hydrostatic stress tensor, which is represented in Voigt notation as

$$\boldsymbol{\sigma}_{\rm H} = \boldsymbol{C\delta} = \begin{pmatrix} C_{11} & C_{12} & C_{13} & C_{14} & C_{15} & C_{16} \\ C_{12} & C_{22} & C_{23} & C_{24} & C_{25} & C_{26} \\ C_{13} & C_{23} & C_{33} & C_{34} & C_{35} & C_{36} \\ C_{14} & C_{24} & C_{34} & C_{44} & C_{45} & C_{46} \\ C_{15} & C_{25} & C_{35} & C_{45} & C_{55} & C_{56} \\ C_{16} & C_{26} & C_{36} & C_{46} & C_{56} & C_{66} \end{pmatrix} \begin{pmatrix} \delta \\ \delta \\ \delta \\ 0 \\ 0 \\ 0 \end{pmatrix} = \begin{pmatrix} \sigma_{\rm H} \\ \sigma_{\rm H} \\ \sigma_{\rm H} \\ 0 \\ 0 \\ 0 \end{pmatrix}. \quad (14)$$

Therefore, the stiffness tensor components must satisfy the following conditions simultaneously:

$$\begin{cases} C_{11}+C_{12}+C_{13} = C_{12}+C_{22}+C_{23} = C_{13}+C_{23}+C_{33}, \\ C_{14}+C_{24}+C_{34} = 0, \\ C_{15}+C_{25}+C_{35} = 0, \\ C_{16}+C_{26}+C_{36} = 0. \end{cases} \quad (15)$$

It is known that the stiffness tensor depends on the crystal symmetry (Laue group) and the independent components can be further reduced by taking crystal symmetry into consideration. The stiffness tensor matrices in all 11 Laue groups are listed in Appendix *E* of the book by Nye (1985). Based on the relationship between these components, it is found that equation (15) is only satisfied for the stiffness tensor of cubic crystals $\boldsymbol{C}_{\rm cubic}$ [equation (16)], where the relationship between the components is displayed in equation (17):

$$\boldsymbol{C}_{\rm cubic} = \begin{pmatrix} C_{11} & C_{12} & C_{12} & 0 & 0 & 0 \\ C_{12} & C_{11} & C_{12} & 0 & 0 & 0 \\ C_{12} & C_{12} & C_{11} & 0 & 0 & 0 \\ 0 & 0 & 0 & C_{44} & 0 & 0 \\ 0 & 0 & 0 & 0 & C_{44} & 0 \\ 0 & 0 & 0 & 0 & 0 & C_{44} \end{pmatrix}, \quad (16)$$

$$\begin{cases} C_{11} = C_{22} = C_{33}, \\ C_{12} = C_{13} = C_{23}, \\ C_{41} = C_{42} = C_{43} = C_{51} = C_{52} = C_{53} = C_{61} = C_{62} = C_{63} = 0. \end{cases} \quad (17)$$

As a consequence, the deviatoric stress tensor in cubic crystals can be calculated by direct multiplication of the stiffness tensor and deviatoric strain tensor, although this results in an approximation of the real deviatoric stress tensor in non-cubic crystals.

Acknowledgements

We thank Mr C. W. Fan for website maintenance.

Funding information

This work was supported by the National Natural Science Foundation of China, Major Research Plan (grant Nos. 51901026, 91860109, 51927801 and 51671154), the National Key Research and Development Program of China (grant Nos. 2016YFB0700404 and 2016YFB1100103), the Natural Science Basic Research Plan in Shaanxi Province of China (grant No. 2020JM-239), the Fundamental Research Funds for the Central Universities (CHD Nos. 300102319301 and 300102319208), and the open project of the State Key Laboratory for Mechanical Behavior of Materials (grant No. 20171907). Beamline 12.3.2 of the Advanced Light Source is supported by the Director, Office of Science, Office of Basic Energy Sciences, Materials Science Division, of the US Department of Energy under contract No. DE-AC02-05CH11231 at LBNL. HRW acknowledges support from the NSF (EAR 1343908) and DOE (DE-FG02-05ER15637).

References

Bachmann, F., Hielscher, R. & Schaeben, H. (2010). *Solid State Phenom.* **160**, 63–68.
Bunge, H.-J. (1969). *Mathematische Methoden der Texturanalyse.* Berlin: Akademie-Verlag.
Campbell, J. W. (1995). *J. Appl. Cryst.* **28**, 228–236.
Chen, K., Dejoie, C. & Wenk, H.-R. (2012). *J. Appl. Cryst.* **45**, 982–989.
Chen, K., Huang, R., Li, Y., Lin, S., Zhu, W., Tamura, N., Li, J., Shan, Z.-W. & Ma, E. (2020). *Adv. Mater.* **32**, 1907064.
Chen, K., Kunz, M., Li, Y., Zepeda-Alarcon, E., Sintubin, M. & Wenk, H. R. (2016). *Geophys. Res. Lett.* **43**, 6178–6185.
Chen, K., Kunz, M., Tamura, N. & Wenk, H. R. (2015). *Geology*, **43**, 219–222.
Chen, K., Tamura, N., Kunz, M., Tu, K. N. & Lai, Y. S. (2009). *J. Appl. Phys.* **106**, 023502.
Chen, K., Tamura, N., Tang, W., Kunz, M., Chou, Y. C., Tu, K. N. & Lai, Y. S. (2010). *J. Appl. Phys.* **107**, 063502.

electronic reprint

Chen, X., Dejoie, C., Jiang, T., Ku, C. S. & Tamura, N. (2016). *MRS Bull.* **41**, 445–453.
Dejoie, C., Sciau, P., Li, W., Noé, L., Mehta, A., Chen, K., Luo, H., Kunz, M., Tamura, N. & Liu, Z. (2014). *Sci. Rep.* **4**, 4941.
Do, X., Li, D., Zhang, A., He, B., Zhang, H. & Doan, T. (2013). *J. Laser Appl.* **25**, 2–7.
Engler, O. & Randle, V. (2009). *Introduction to Texture Analysis: Macrotexture, Microtexture, and Orientation Mapping.* Boca Raton: CRC Press.
Guo, H., Chen, K., Oh, Y., Wang, K., Dejoie, C., Syed Asif, S. A., Warren, O. L., Shan, Z. W., Wu, J. & Minor, A. M. (2011). *Nano Lett.* **11**, 3207–3213.
He, Y. & Jonas, J. J. (2007). *J. Appl. Cryst.* **40**, 559–569.
Kocks, U. F., Tomé, C. N. & Wenk, H.-R. (1998). *Texture and Anisotropy: Preferred Orientations in Polycrystals and their Effect on Materials Properties.* Cambridge University Press.
Kou, J., Chen, K. & Tamura, N. (2018). *Scr. Mater.* **143**, 49–53.
Kunz, M., Tamura, N., Chen, K., MacDowell, A. A., Celestre, R. S., Church, M. M., Fakra, S., Domning, E. E., Glossinger, J. M., Kirschman, J. L., Morrison, G. Y., Plate, D. W., Smith, B. V., Warwick, T., Yashchuk, V. V., Padmore, H. A. & Ustundag, E. (2009). *Rev. Sci. Instrum.* **80**, 035108.
Laughier, J. & Filhol, A. (1983). *J. Appl. Cryst.* **16**, 281–283.
Lee, L., Tang, S.-Y., Chen, J.-H., Su, T.-Y., Chen, H.-C., Lin, C.-H., Chiang, C.-Y., Chiu, S.-J., Ku, C.-S., Shen, J.-L., Wang, Z. M. & Chueh, Y.-L. (2020). *ACS Appl. Mater. Interfaces*, **12**, 32041–32053.
Li, R., Xie, Q., Wang, Y.-D., Liu, W., Wang, M., Wu, G., Li, X., Zhang, M., Lu, Z., Geng, C. & Zhu, T. (2018). *Proc. Natl Acad. Sci. USA*, **115**, 483–488.
Li, Y., Chen, K., Narayan, R. L., Ramamurty, U., Wang, Y., Long, J., Tamura, N. & Zhou, X. (2020). *Addit. Manuf.* **34**, 101220.
Li, Y., Chen, K. & Tamura, N. (2018). *Mater. Des.* **150**, 171–181.
Li, Y., Qian, D., Xue, J., Wan, J., Zhang, A., Tamura, N., Song, Z. & Chen, K. (2015). *Appl. Phys. Lett.* **107**, 181902.
Li, Y., Wan, L. & Chen, K. (2015). *J. Appl. Cryst.* **48**, 747–757.
Liu, H. & Liu, J. (2012). *J. Appl. Cryst.* **45**, 130–134.
Liu, W., Ice, G. E., Larson, B. C., Yang, W., Tischler, J. Z. & Budai, J. D. (2004). *Metall. Mater. Trans. A*, **35**, 1963–1967.
Lupinacci, A., Chen, K., Li, Y., Kunz, M., Jiao, Z., Was, G. S., Abad, M. D., Minor, A. M. & Hosemann, P. (2015). *J. Nucl. Mater.* **458**, 70–76.
Ma, E. Y., Cui, Y. T., Ueda, K., Tang, S., Chen, K., Tamura, N., Wu, P. M., Fujioka, J., Tokura, Y. & Shen, Z. X. (2015). *Science*, **350**, 538–541.
Matthies, S., Wenk, H.-R. & Vinel, G. W. (1988). *J. Appl. Cryst.* **21**, 285–304.
Noyan, I. C. & Cohen, J. B. (2013). *Residual Stress: Measurement by Diffraction and Interpretation.* Heidelberg: Springer.
Nye, J. F. (1985). *Physical Properties of Crystals: Their Representation by Tensors and Matrices*. Oxford University Press.
Robach, O., Kirchlechner, C., Micha, J. S., Ulrich, M. O., Biquard, X., Geaymond, M. O., Castelnau, O., Bornert, M., Petit, J., Berveiller, S., Sicardy, O., Villanova, J. & Rieutord, F. (2014). *Strain and Dislocation Gradients from Diffraction: Spatially Resolved Local Structure and Defects*, edited by R. Barabash & G. Ice, pp. 156–204. Singapore: World Scientific.
Soyer, A. (1996). *J. Appl. Cryst.* **29**, 509.
Strelcov, E., Tselev, A., Ivanov, I., Budai, J. D., Zhang, J., Tischler, J. Z., Kravchenko, I., Kalinin, S. V. & Kolmakov, A. (2012). *Nano Lett.* **12**, 6198–6205.
Tamura, N. (2014). *Strain and Dislocation Gradients from Diffraction: Spatially Resolved Local Structure and Defects*, edited by R. Barabash & G. Ice, pp. 125–155. Singapore: World Scientific.
Wenk, H.-R., Chandler, B. C., Chen, K., Li, Y., Tamura, N. & Yu, R. (2020). *Geophys. J. Int.* **222**, 1363–1378.
Wenk, H.-R., Matthies, S., Donovan, J. & Chateigner, D. (1998). *J. Appl. Cryst.* **31**, 262–269.
Xue, J., Zhang, A., Li, Y., Qian, D., Wan, J., Qi, B., Tamura, N., Song, Z. & Chen, K. (2015). *Sci. Rep.* **5**, 14903.
Zhou, G., Kou, J., Li, Y., Zhu, W., Chen, K. & Tamura, N. (2018). *Quantum Beam Sci.* **2**, 13.
Zhou, G., Zhu, W., Shen, H., Li, Y., Zhang, A., Tamura, N. & Chen, K. (2016). *Sci. Rep.* **6**, 28144.

electronic reprint